"Design, synthesis, structural and porosity characterization of novel functional MOFs with amino acid azole based ligands"

Submitted by

Dr. Adarsh Nayarassery Narayanan

Under the supervision of *Prof. Dr. Yann Garcia*

Institute of Condensed Matter and Nanosciences
MOST unit
Université Catholique de Louvain,
Place L. Pasteur 1,
1348 Louvain-la-Neuve,
Belgium

Introduction

Metal-organic frameworks (MOF) are polymeric crystalline materials that are formed by the supramolecular self-assembly of metal ions and ligands driven by metal-ligand coordination bonding.[1] Due to their aesthetic structures, and intriguing functional properties such as gas storage/separation, catalysis, magnetism, drug delivery, luminescence, non-linear optics porosity or zeolitic behaviour etc., these functional materials received a great attention of the scientific community.[1] The prominent features of the designed ligands are the presence of diverse potential coordinating groups such as carboxylic acid and triazole/tetrazole on the same framework as well as the inherent flexibility of the ligand backbone. We have designed a series of triazole/tetrazole ligands with chiral (L-amino acid) and non-chiral backbone (Scheme 1).

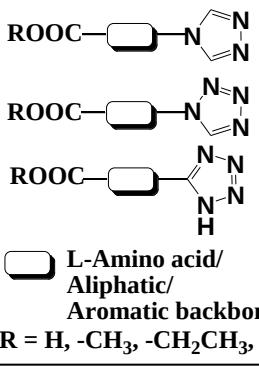

Scheme 1

The general objectives of this basic research project can be summarized as follows: (***19th January 2012 – 18th July 2013***)

1) Obtaining new MOFs and fully characterize them both analytically and structurally (***January 2012-June 2013***).

2) Perform a full porosity characterization (He, N_2 and Hg) and robustness to thermal treatment (TGA) and various guest solvent molecules (***January 2012-May 2013***).

3) Correlate crystal structures with physical properties (in particular porosity and spin crossover behaviour of Fe^{II} MOFs) to gain novel insights towards crystal engineering of these important materials (***January 2012-July 2013***).

4) Final report (***September 2013***).

2. Results and discussion

2.1 Synthesis and characterization of 1,2,4-triazole/tetrazole ligands

We have deigned and successfully synthesized a new series of 1,2,4-triazole-carboxylic acid, triazole-ester ligands, tetrazole ligands derived from chiral L-amino acid and achiral aromatic/aliphatic compounds, (Scheme 2) and fully characterized by various methods such as NMR, elemental analysis, FT-IR, ESI-Mass etc.. The ligands **L1-L4** were synthesized by following our reported method.[2] A schematic representation of synthesis of **L1-L7** is shown in Scheme 3.

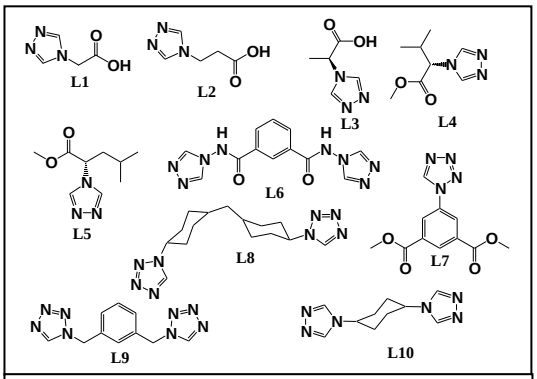

Scheme 2

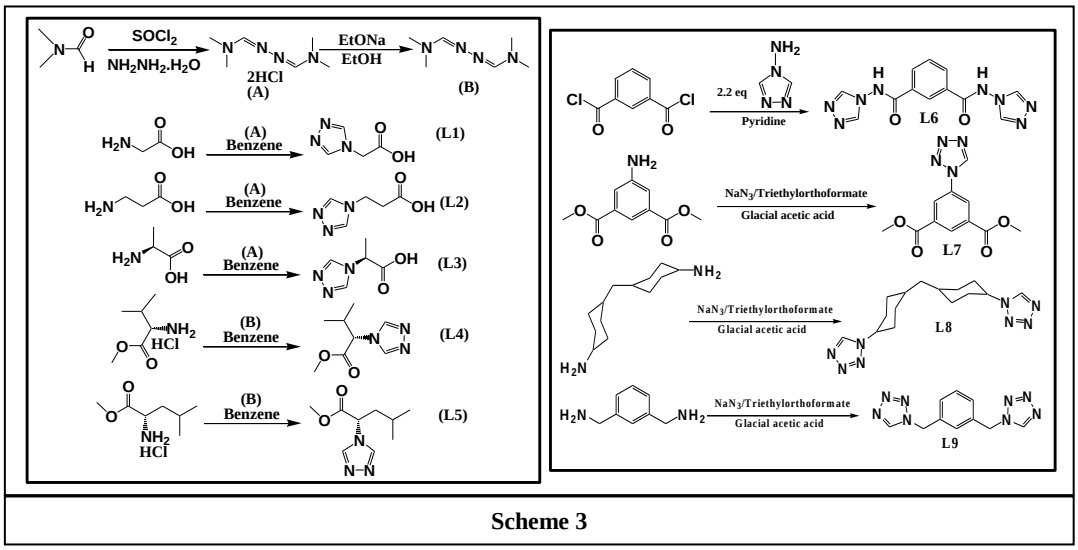

Scheme 3

2.2 Synthesis and characterization of functional MOFs for sorption and SCO phenomena *(Highlights of few key results)*[3]

2.2.1 Entrapment of Mercury in a Single-Walled Metal-Organic Nanotube (SWMONT)

Significant expose to all forms of mercury can lead to a variety of health problems including respiratory, immune, dermatologic, and developmental sequel.[3a] Mercury can also lead to severe problems when it comes into contact to a tissue in sufficient concentration, the two main effects being neurological and renal disturbances.[3b] Thus, it is very important to propose materials able to behave as mercury sponges, particularly for children safety for instance due to household poisoning cases from mercury brought from school.[3a] Although various methods have been proposed to remove mercury from waste water including ion exchange,[4a] membrane filtration,[4b] adsorption,[4c] chelate precipitation,[4d] and photo-reduction,[4e] there are very few materials able to store metallic mercury.[5]

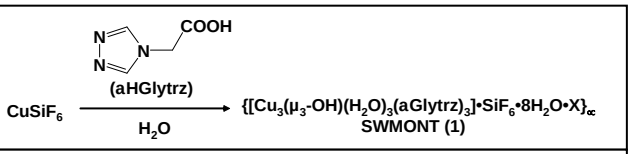

Scheme 4

As a part of our ongoing research in synthesizing novel MOFs,[6] we were interested in an active storage material for mercury.[6a-6c] Recently we have reported a MOF nanoball obtained by the self-assembly of $Cu(BF_4)_2$ with 4H-1,2,4-Triazol-4-yl-acetic acid **L1** (**αHGlytrz**).[6c] Among various factors affecting the resultant supramolecular structure, the ligating topology of **αHGlytrz** and the nature of anion are crucial.[7] Therefore we have reacted **αHGlytrz** with $CuSiF_6$, in water in 1:1 molar ratio, where the divalent anion has a symmetrical octahedral shape. The reaction resulted in the formation of needle shaped blue colored single crystals of **1**, identified by single crystal X-ray diffraction as a single-walled metal organic nanotube (SWMONT)[8] namely $\{[Cu_3(\mu_3\text{-}OH)(H_2O)_3(\mathbf{Glytrz})_3]\bullet SiF_6 \bullet 8H_2O\bullet X\}_\infty$ (**1**), X = disordered lattice water molecules (Scheme 4). Such kind of highly robust, structurally diverse and functionally intriguing MOF nanotubular materials, with various topologies and porosities, have been found useful for gas storage/separation, catalysis, as molecular switches, drug carrier etc.[9] Although they have not been much explored so far, SWMONTs show very interesting features such as controlled sizes, shapes, electronic states, and robustness. In this section, we present a novel synthetic approach for SWMONT that is obtained by the supramolecular self-assembly of a secondary building unit (SBU).[10] **1** was characterized by elemental analysis, FT-IR, thermogravimetric analysis, scanning electron microscopy (SEM), atomic force microscopy (AFM), single crystal and powder X-ray diffraction methods. The strong broadband around 1735 cm^{-1} identified for the -C=O group by FT-IR spectroscopy for **αHGlytrz** is shifted to 1645 cm^{-1} in **1** due to its coordination to Cu^{II}. Two intense bands at 746 and 482 cm^{-1} are assigned to the vibration of SiF_6^{2-} anion. The crystals of **1** were insoluble in almost all common solvents indicating their coordination polymer nature; the crystals were stable under ambient conditions. Single crystal of **1** suitable for X-ray diffraction was grown from a water solution containing $CuSiF_6$ and **αHGlytrz** in a 1:1 stoichiometric ratio by slow evaporation. We could also synthesize the same crystals by using electrochemical method (EC) in better yields and shorter time compared the conventional slow evaporation method. The EC method is based on the delivery of the metal ions by positively polarizing an electrode in a solution containing the linkers needed for the synthesis. The metal ions

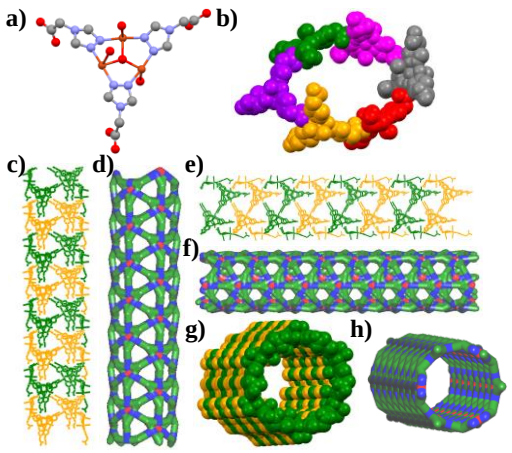

Figure 1: Crystal structure illustration of **1**: a) triazole-carboxylate SBU; b) 'crown ether' like metallo-macrocyle, wherein the SBUs are shown in various colors; c)-h) view of SWMONT **1** under various crystallographic axis (Figures 1c-1d: a axis ; 1e-1f: b axis, 1g-1h: c axis) wherein adjacent macrocycles are shown in orange and green color; TOPOS[13] representation of **1** is shown in d), f) and h).

released from the electrode react with the linker forming a layer and partially precipitating in the solution.[11a] The amount of material precipitated or attached to the surface can be tuned changing the solution composition and the temperature.[11b] Thanks to the EC method, coordination compounds can be deposited on porous support and used as filter and membranes.[11c]

Single crystal X-ray diffraction (XRD) analysis of **1** revealed a centrosymmetric trigonal *P*31*c* space group. The asymmetric unit comprises a trinuclear Cu^{II} SBU obtained from three Cu^{II}, one hydroxyl group (OH^-), tri-coordinated with three Cu^{II}, three ligand molecules (also coordinated with Cu^{II} via a bidentate chelating triazole moiety and monodentate coordinating carboxylate O), three water molecules (also coordinated to Cu^{II}) (Fig. 1a), one SiF_6^{2-} anion and four lattice water molecules, of which two are located on the 3-fold axis. The Cu^{II} metal center displays a slightly distorted square pyramidal geometry [∠O–Cu–N = 91.0(4)-95.3(5)º, ∠O–Cu–O = 92.8(4)-93.8(5)º]; the equatorial positions of the metal center are coordinated by the triazole N and carboxylate O atoms of the ligand and the apical positions are occupied by a water molecule, which leads to the formation of trinuclear Cu^{II} SBU (Fig 1a, Scheme 2). In fact, the trinuclear Cu^{II} SBU is disordered around the 3-fold symmetry axis. The extended coordination of such six trinuclear Cu^{II} SBU (via carboxylate O atom of **Glytrz** with Cu^{II}) leads to the formation of a 'crown ether' like metallo-macrocycle which is the primary supramolecular synthon (Fig. 1b).

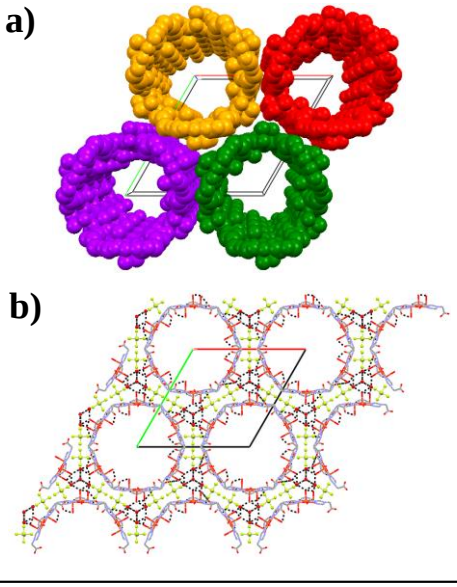

Figure 2: Crystal structure view of **1**: a) hexagonal close packing of the SWMONT **1** viewed down the c-axis. b) Occlusion of counter anion SiF_6^{2-} and lattice included water molecules on the outer space of the SWMONT.

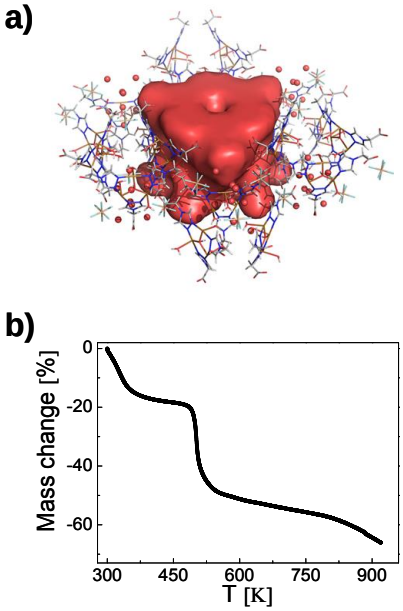

Figure 3:. a) Small (shown with red balls) and large cavities (giant triangular shape) found in the crystal structure of **1**; b) TGA plot of **1**

Such metallo-macrocycle is further extended by the carboxylate moiety of the SBUs which leads to the formation of a SWMONT having an effective pore size of ~ 14.12 Å and an outer diameter of 21.48 Å (Fig. 1c-h). Such SWMONTs are packed in a hexagonal fashion (Fig. 2a) within the crystal lattice sustained by various H-bonding interactions with the lattice water molecules and the SiF_6^{2-} anion [O···O = 2.572–3.163Å; ∠O–H···O = 116.27-175.93°; O···F = 2.788–2.989Å] (Fig. 2b). Outside the first coordination sphere, no solvent molecules could be located; the SQUEEZE algorithm (Platon)[12] was therefore used to accommodate the disordered lattice water molecules (X). A total of 406e^- distributed over one large cavity (2206$Å^3$ = 34% of unit cell volume, 382e^-) corresponding to X = 6 and 6 very small cavities (7$Å^3$, 4e^-), which are too small to host water molecules (expected volume ~40$Å^3$) were estimated (Fig. 3a). Thermogravimetric analysis (TGA) showed a weight loss of 19.18% up to 204°C attributed to 10 water molecules (3 coordinated + 7 lattice included ordered H_2O) (Fig. 3b) which was confirmed by elemental analysis.

AFM images show spherical particles with an average height of 2.14-2.28(2) nm, thereby confirming the nanotubular morphology. Interestingly, an outer diameter of ~ 2.148 nm was found in the crystal structure of **1**, and a tubular arrangement was seen in SEM experiments which revealed the crystalline nature of **1**. The thermal stability and crystalline phase purity of the bulk crystals of **1**, was determined by both TGA and X-ray powder diffraction (XRPD). The simulated XRPD pattern obtained from single crystal data and bulk crystals of **1** are matching, indicating high crystalline phase purity, which was confirmed by SEM analysis. A good correspondence with these patterns was also found for the pattern of a dried sample after heating at 150°C, which indicates the robustness of the SWMONT **1**, which was confirmed by TGA at 150°C. Mercury intrusion porosimetry (MIP) as a function of applied pressure was undertaken to evaluate the meso- and macroporosity of **1**. The aim of this experiment was double. First of all, MIP is a very useful and powerful technique to investigate the porosity of materials that contain pores larger than 7.5 nm (pore size and pore volume). This is extremely precious in terms of full porosity characterization, where $N_{2(g)}$ adsorption becomes insufficient, especially regarding large pores. Secondly, this measurement can also tell whether mercury can remain entrapped inside the material or if it will be expelled upon pressure release. In our case, we noted that mercury remains entrapped, after pressure relieve back to atmospheric pressure, suggesting an affinity of the material towards mercury. The differential intrusion curve shows four distinct steps that correspond to pore sizes of 24 nm, 120 nm, 14 nm and 11 nm according to the Washburn equation[14] (Fig. 4). The major contribution probably arises from interparticular porosity, confirming the regular dimensions of the formed particles. Usually, intrusion-extrusion phenomena *via* reversible large pore to narrow pore transition triggered by external pressure are expected. However, due to the rigid nature of **1**, an irreversible behavior was observed (Fig. 4). Indeed, a large part of the entrapped mercury was not retrieved after pressure relieves down to 0.36 MPa, indicating that this material shows mercury storage properties. This was further confirmed visually by the colour change of the deep blue crystals that turned grey. Interestingly, two steps were detected at 100 and 125 MPa in the cumulative intrusion curve. These steps correspond to pore size of 15 and 12 nm according to the Washburn equation,[14] which were also found in the pore size distribution described above. On release of the pressure, an hysteresis effect is observed with release of Hg from narrow pores, which remain however trapped in large pores (24 nm and 120 nm).

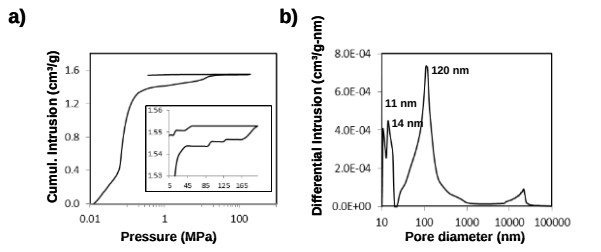

Figure 4: a) Intrusion curve (inset shows the enlarged part of the graph between 20 and 200 MPa revealing small steps) and b) corresponding pore size distribution of the SWMONT **1**.

Conclusion: In summary, the supramolecular self-assembly of SBUs unit provided an unprecedented SWMONT derived from a copper salt and a simple triazole-carboxylate ligand. Desolvation of the lattice water indicated the thermal robustness and microporosity of the SWMONT which displayed, in its crystal structure, open pores as large as zeolites.[15] More interestingly, this material showed entrapment and storage of inorganic mercury even after pressure relieve which is confirmed by sorption experiment; a property highly beneficial for mercury storage.

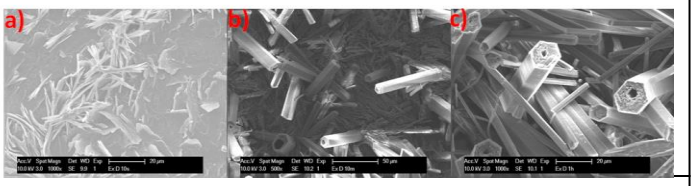

Figure E1: SEM micrographs of the SWMONT **1** layer deposited at constant potential (1 V vs Ag), after a time interval of 10 s, 10 min. and 1 h. (experiment 1, 2 and 3)are shown in figure a), b) and c), respectively.

Experimental section on EC method* (*this work has been done during project extension period)
A solution containing 30mg of **αHGlytrz** and 42 mg of $(NH_4)_2SiF_6$in 10 ml distilled water was used as electrolyte. $(NH_4)_2SiF_6$ has been added in order to have the SiF_6^{2-} anion in solution but no copper cation. Electrochemical

experiments were run with a galvanostat/potentiostat in a three electrode setup using polished copper plates or copper coated wafer substrates as working electrodes, a silver wire as reference and a palladium counter electrode.

Various experiments have been carried out to study the EC synthesis of SWMONT **1**. It is important to perform an exploratory study on the synthetic parameters which effect the formation of **1**.

Experiment 1-3: It is revealed that if the current applied is too high, the obtained phase is not nanotubes but sheet like morphology. The growth at constant voltage, corresponding to low current, is shown in Fig. E1: in the first stage the surface mainly gets covered with flakes with a consequent decrease in the current. After all the surface is covered with these flakes, nanotubes start nucleating and growing. The nucleation and growth continue even after all the surfaces are covered and no sign of detachment during deposition were observed in any of the samples. Being brittle, if the layers are grown too thick they are prone to be scratched away. The expected hexagonal structure is evident and in some cases the tubes are big enough to be hollow (Fig. E1).

Table E1: Experimental details of electrochemical synthesis of SWMONT **1**

Experiment	Current	Time	Temperature	Result
1	75 mA	10 min	60°C	Tubes and flakes
2	100 mA/cm2	1 min	60°C	Flakes
3	4.2 mA	3 h	60°C	Tubes
4	4.2 mA	3 h	60°C	Islands. Remark: the solution had 1/3 of the $(NH_4)_2SiF_6$ required
5	1 V .1	1 min	60°C	Almost nothing
6	1 V .2	1 min	60°C	Well covered
7	1 V	10 min	60°C	Over covering
8	6 mA	3 h	60°C	Yield study

Similar kind of nanotubular morphology was also observed in experiment 3-4, wherein the synthesis was performed in a time interval of 3 h (galvanisation) and a concentration of $(NH_4)_2SiF_6$ of 1/3 with respect to the ligand molecule. In fact by keeping a constant current the concentration of copper on the electrode is constant and the nanotubes synthesized are well grown and have homogeneous dimensions. In order to calculate the yield with this technique, the synthesis has been run for 3 hours at 6 mA. The amount of copper released is not stoichiometric with the SiF_6^{2-} anion since part of the metal is lost due to reduction on the counter electrode. The amount of MOF collected from the solution is 36 mg (0.0255 mmol), and another 25.2 mg (0.0178 mmol) could be recovered scratching the electrode. The total amount of material synthesized is therefore 61.2 mg, corresponding to a yield of 18.3%. We have also performed the SEM and the corresponding EDAX data of the flakes and nanotubes exclusively. It is revealed from the PXRD data that SWMONT of the materials obtained from EC method and conventional method that atomic estimation for light elements is not exact due to the low intensity of the peaks. The presence of Pt and Pd is due to the coating deposited to increase the conductivity to take SEM pictures.

2.2.2 Cu^{II} Metal-Azole frameworks derived from a simple triazole-carboxylic acid ligand (L2): Structures and Magnetic properties

The design and construction of polymeric metal-organic compounds, the so called metal organic frameworks (MOFs),[1] are of ever increasing interest of the scientific community. Reasons behind such great curiosity are due to their aesthetic structures and intriguing functional properties such as gas storage/separation, catalysis, magnetism, drug delivery, luminescence, non-linear optics, porosity, zeolitic behaviour, *etc*.[1] However, rational engineering and controlled preparation

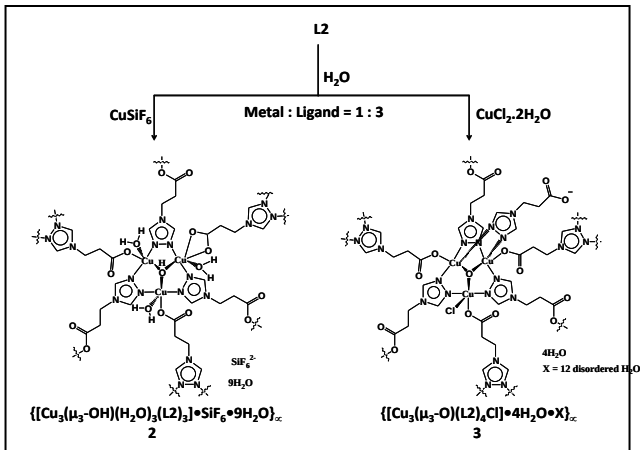

Scheme 5

of such materials is ever challenging. Supramolecular chemistry[17] and crystal engineering[18] approaches are the main tools for rational design of such materials. One of the most effective strategies is the self-assembly reaction of different metal ions (nodes) with predesigned organic ligands (building blocks), which is mainly driven by metal-ligand coordination bonds.[19] Moreover, various secondary intra- and/or intermolecular interactions, *e.g.* H-bonds,[20] $\pi\cdots\pi$ stacking,[21] C–H$\cdots\pi$ interactions,[22] *etc.*, also affect the final supramolecular structures of MOF. These interactions become crucial for the aggregation of polynuclear discrete subunits or low-dimensional motifs into higher-dimensional frameworks. Thus, the nature of a ligand is of great importance for the creation of MOFS.[23] Various ligands, anchoring different functionalities such as carboxylate,[1a] pyridine,[7] polyfuctional system,[24] *etc.*, have been used for MOFs. On the other hand, MOFs derived from azole ligands, the so called metal-azole frameworks, in particular amino acids and azole-carboxylate ligands, have still been poorly explored.[25] Combination of both azole and carboxylic acid in a single molecule is an attractive design strategy for the creation of new MAFs. Such ligands might form SBUs,[10] which able to form sub-structural motifs within the resultant crystal structure. Furthermore, such ligands might exhibit an internetwork supramolecular recognition properties, which, in turn, might lead to the formation of a more robust supramolecular architecture and ensure guest entrapment within the interstitial voids *via* various intermolecular interactions.

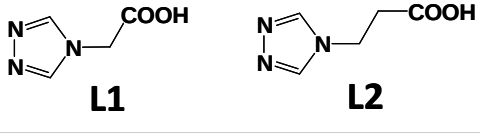

Chart 1

Krautscheid and co-workers exploited a triazole-carboxylate ligand methyl-5-(pyridin-4-yl)-(4*H*-1,2,4-triazol-4-yl)isophthalate for the generating a novel microporous Cu^{II} MOF, exhibiting high H_2 and CO_2 adsorption capacities at ambient pressure.[26] Recently a new pillaring strategy for the construction of novel structural MOFs, derived from triazole-carboxylate ligands, has been reported.[27] Interestingly, triazole-carboxylate ligands have been utilized for design, synthesis, and facile tuning of a new series of **rht**-MOFs.[28] Several groups also explored various triazole-carboxylate ligands for the functional MOFs.[29] As a part of our ongoing research on synthesis of novel MOFs, we are fascinated in studying the supramolecular structural diversities in MOFs and their affecting forces (*e.g.* H-bonding, anions, ligating topology, *etc.*) as well as functional properties (*e.g.* spin-crossover behaviour, sorption properties, *etc.*[30]). Recently we have reported a remarkable three dimensional chains of nanoballs derived from $Cu(BF_4)_2$ and 2-(4*H*-1,2,4-triazol-4-yl)acetic acid (**L1**) (Chart 1). The crystal structure analysis revealed that the self-assembly of the C_3-symmetric, μ^3-O bridged triangular tricopper SBU is the main driving force for the formation of nanoballs with a void size of ~1 nm and total solvent accessible volume of 4477.5 $Å^3$, which accounts for 48% of the cell volume.[30a] We have also reported a novel chiral helicate, derived from **L1** and $CdCl_2$.[30b] Encouraged by these results and with the aim to obtain new MAFs, a close homologue of **L1**, 3-(4*H*-1,2,4-triazol-4-yl)propanoic acid (**L2**) (Chart 1), was involved in the reaction with $CuSiF_6$ and $CuCl_2$, respectively. It should be noted, that **L2** is a relatively more flexible ligand compared to **L1** due to a longer spacer between the triazole and carboxylic functions. This might be crucial for the creation of new supramolecular aggregates.

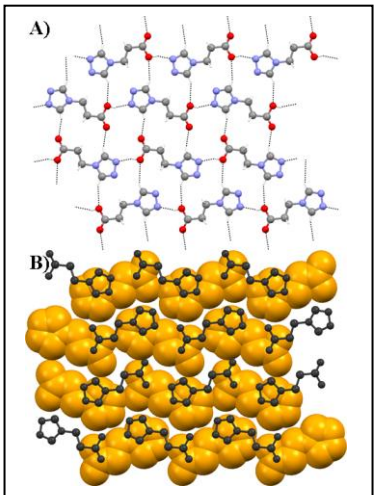

Figure 5: Ball and stick plot of the 2D sheet of **HL2** (**A**) and their offset packing, where adjacent sheets are shown in orange spacefill and black ball and stick plots, respectively (**B**). H-atoms in **B** were omitted for clarity.

The ligand **L2** was prepared by reacting *β*-alanine with the *N*,*N*′-dimethylformamide azine dihydrochloride (DMFA·2HCl).[2] Reaction of **L2** with $CuSiF_6$ and $CuCl_2$, respectively, in water lead to heteroleptic complexes $\{[Cu_3(\mu_3\text{-}OH)(H_2O)_3(\mathbf{L2})_3]SiF_6\cdot 9H_2O\}_\infty$ (**2**) and $\{[Cu_3(\mu_3\text{-}O)(\mathbf{HL})(\mathbf{L2})_3Cl]\cdot 0.36CH_2Cl_2\cdot 8.28H_2O\}_\infty$ (**3**) (Scheme 5). The IR spectra of **L2** contains characteristic bands at 1720 and 3124 cm^{-1}, corresponding to the C=O and CH fragments of the carboxylic and triazole groups, respectively. The IR spectra of **2** and **3** each contains a broad band for the water molecules centered at 3390–3400 cm^{-1}. A band for the triazole CH groups was found at 3122 and 3112 cm^{-1} in the spectra of **2** and **3**, respectively. The main difference involves the absorption bands of the C=O group. In the spectra of **2** and **3** there is a characteristic band for the C=O group, which is about 120 cm^{-1} shifted to low frequences. This band corresponds to the deprotonated carboxylic fragment. The spectrum of **3** also contains a second band for the C=O group, which is in the same range as it was found for the parent ligand **L2**, corresponding to the protonated carboxylic function. The IR spectrum of **1** also contains a band at about 725 cm^{-1}, corresponding to the SiF_6^{2-} anion. The diffuse reflectance spectrum of **L2** exhibits absorption bands exclusively in the UV region, corresponding to intraligand transitions. The same bands were also observed in the spectra of **2** and **3**. However, they are red-shifted. The absorption spectrum of **2** exhibits a broad absorption band in the range 450–900 nm corresponding to the *d*-*d* transitio). The spectrum of **3** contains two broad absorption bands at 400–1000 nm, which also correspond to the *d*-*d* transition. The thermal properties of **L2**, **2** and **3** in the dynamic air atmosphere were studied by means of simultaneous TG/DTA analyses in order to determine their respective stability. The molecule of **L2** is stable up to 200 °C and decomposed in two clearly defined steps. The formation of carbon after the first decomposition step is observed, which completely burns after the second step. The thermal decomposition process reveals two clearly defined *endo*thermic effects at 182 and 248 °C, and one *exo*thermic effect at 525 °C. Molecules of **2** and **3** decomposed in four and three steps respectively. The first decomposition step of **2** and **3** corresponds to the loss of five and two water molecules, respectively. The thermal decomposition process of **2** and **3** reveals a number of *endo*thermic effects, and one clearly defined *exo*thermic effect at 450 and 495 °C, respectively.

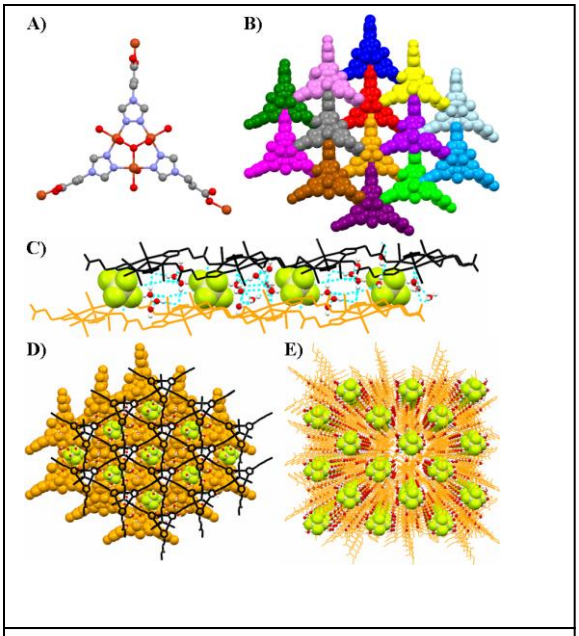

Figure 6: Crystal structure of **2**: ball and stick plot of SBU (**A**); spacefill plot of the 2D coordination grid architecture, formed by SBUs (**B**); spacefill, and ball and stick plot of the entrapped SiF_6^{2-} anions and water molecules within the interstitial space of two adjacent grids (**C**); spacefill, and ball and stick plot of an off-set packing of 2D coordination grids, sustained by various hydrogen bonding interactions, involving SiF_6^{2-} anions and water molecules (**D**); spacefill and wireframe plot of the overall packing of 2D grids and entrapped of SiF_6^{2-} anions and water molecules (**E**).

Crystals of **L2** were obtained from methanol solution with ether diffusion. Crystals of **2** were obtained by slow evaporation of its solution in water, while crystals of **3** were grown from an aqueous CH_2Cl_2 (90:10, v/v) solution. The structures of **L2** and **2** were refined in the space group $P2_1/c$, while the structure of **3** was refined in the space group $C2/c$. It should be noted that for each **2** and **3** several crystals have been tested by a single crystal X-ray analysis, confirming the uniformity of the crystallized sample. The molecule **L2** is essentially planar with the dihedral angle value between the planes formed by the triazole and carboxylic functions being 3.56(9)°. The structure of **L2** is stabilised by two intermolecular hydrogen bonds N···H–O, formed between one of the nitrogen atoms of the triazole ring and the OH hydrogen atom of the carboxylic fragment (Fig. 5). As a result of these intermolecular interactions, 1D polymeric chains are formed. These chains are further linked to each other through C–H···O=C and C–H···O–H interactions, formed between the CH hydrogen atoms of the triazole ring and oxygen atoms of the

carboxylic group. These interchain interactions leads to the formation of 2D sheets, which are tightly packed to each other due to $\pi\cdots\pi$ interactions between triazole rings (Fig. 5). The crystal structure of **2** exhibits a triangular domain [$Cu_3(\mu_3$-OH)$(H_2O)_3$(**L2**)$_3$], formed by three Cu^{II} atoms and three deprotonated ligands **L2**, each being coordinated to two metal centers in a bridging μ_2-*N*1,*N*2-fashion (Fig. 6). The center of this domain is occupied by the OH^- group, which is μ_3-coordinated to all Cu^{II} atoms. The coordination spheres of metal ions are completed by the oxygen atom of the coordinated water molecule and one oxygen atom derived from carboxylic functions of neighboring molecules. As a result, all Cu^{II} atoms are in a slighly distorted square pyramidal environment with the water oxygen atom occupying an apical position. The equatorial Cu–N and Cu–O bond lengths are about 2 Å, while the apical Cu–O bond lengths are about 2.3 Å. Due to the bridging coordination mode of the ligands **L2** through the carboxylic and triazole groups, the [$Cu_3(\mu_3$-OH)$(H_2O)_3$(**L2**)$_3$] SBUs form 2D triangular grid architecture. These grids are packed on top of each other in an offset fashion and are stabilized by a number of hydrogen bonds, involving metal bound water molecules, counter anions SiF_6^{2-} and lattice included water molecules (Fig. 6).

The crystal structure of **3** also exhibits a similar triangular domain but with the μ_3-coordinated oxygen atom in the center (Fig. 7). The triazole fragments are also μ_2-*N*1,*N*2-coordinated towards two Cu^{II}. However, the coordination spheres of metal ions are completed exclusively by one of the oxygen atoms derived from carboxylic functions of neighboring molecules .One of the Cu^{II} is additionally coordinated by the chlorine atom, while the other two metal ions are μ_2-*N*1,*N*2-coordinated by the nitrogen atoms of the triazole ring, corresponding to the neutral ligand **L2**. As a result, the Cu^{II} atoms were found in the slightly distorted square pyramidal environment with the equatorial Cu–N and Cu–O bond lengths also being about 2 Å, while the apical Cu–N and Cu–Cl bond lengths are of about 2.2 and 2.5 Å, respectively. The bridging coordination mode of the deprotonated ligands **L2**, similar to the structure of **2**, [$Cu_3(\mu_3$-O)$(H_2O)_3$(**HL2**) (**L2**)$_3$] SBUs also form 2D triangular grid architecture. These 2D grids are packed in an offset fashion, sustained by various hydrogen bonds, involving solvated water and CH_2Cl_2 molecules, metal bound Cl^- anions and non-coordinated carboxylic groups (Fig. 7).

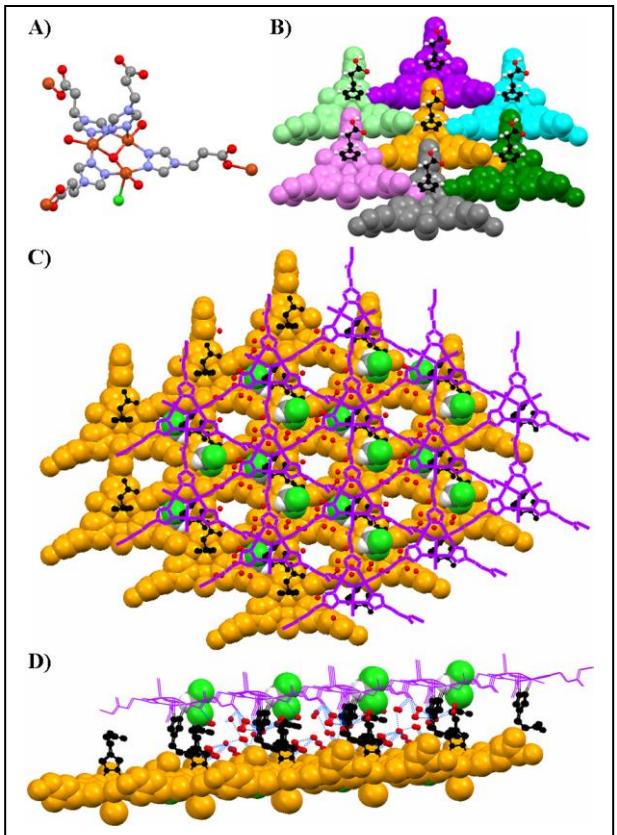

Figure 7: Crystal structure of **3**: ball and stick plot of SBU (**A**); spacefill, and ball and stick plot of the 2D coordination grid architecture, formed by SBUs (**B**); spacefill, and ball and stick plot of the entrapped CH_2Cl_2 and water molecules within the interstitial space of two adjacent grids (**C** and **D**).

Conclusion: We have synthesized two novel MOFs **2** and **3** based on an novel asymmetric bifunctional ligand 3-(4*H*-1,2,4-triazol-4-yl)propanoic acid (**HL2**). According to single crystal X-ray analysis, molecules of **HL2** form 1D polymeric chains through N···H–O intermolecular hydrogen bonds. These chains are further linked to each other through C–H···O=C and C–H···O–H interactions with the formation of 2D sheets. The crystal structures of **2** and **3** each consists of the triangular SBUs [$Cu_3(\mu_3$-X) (**L2**)$_3$] (X = OH for **2** and O for **3**), formed by three Cu^{II} atoms and three μ_2-*N*3,*N*4-coordinated ligands **L2**. The coordination spheres of metal ions are completed by the oxygen atoms derived from carboxylic functions of neighboring molecules. Additionally, Cu^{II} atoms in **2** are coordinated by water molecules. One of the metal ions in **3** is coordinated by the chloride anion and other two cations are bridged by the

triazole function of **HL2** coordinated in a μ_2-*N*3,*N*4-fashion. SBUs in **2** and **3** form a 2D grid architecture, which are packed on top of each other in an offset fashion. Non-coordinated SiF_6^{2-} anions in **2**, CH_2Cl_2 molecules in **3**, and water molecules in both structures are grafted to the 3D network due to hydrogen bonds and weak interactions. Thus, **HL2** was found to be an efficient scaffold for the rational design of, at least, Cu^{II} MOFs by varying anions in the structure of the starting copper source.

2.2.3 Cu^{II} Metal-Azole frameworks derived from a simple triazole-carboxylic acid ligand (L2): Structures and Magnetic properties (*this work has been completed during project extension period: 18th April-18th July)

Microporous coordination polymers (CPs) or MOFs have attracted considerable attention in recent years due to their high thermal stability and porosity.[1] Several research groups have explored CPs and related porous materials for selective gas separation, sensing, catalysis, and host-guest systems. Porous CPs can be synthesised using multidentate ligands such as bis-carboxylate, bis-pyridyl, bis-triazole, bis-tetrazole, mixed ligands etc, to obtain rigid frameworks; however, the final supramolecular archetecture is highly controlled by several factors such as, metal–ligand ratio, solvent of crystallization, nature of ligand, oxidation states of metal centers etc.[1] However, predicting the final topology of CPs derived from flexible ligands is even more a difficult task because of being several supramolecular isomers, with little or no difference in energy, which makes it difficult to predict and control the resultant outcome of crystallization. Therefore the design and synthesis of such supramolecular isomers is still a challenging aspect of crystal engineering.[18] It is evident from various reports that the nature of the ligand is of great importance for the creation of intriguing MOFS.[31] MOFs derived from azole ligands, the so called metal-azole frameworks, in particular bis-triazole/tetrazole ligands, have still been poorly explored.[32] Furthermore, such ligands might exhibit an internetwork supramolecular recognition properties, which in turn, might lead to the formation of a more robust supramolecular host architecture and ensure guest entrapment within the interstitial voids *via* various intermolecular interactions.

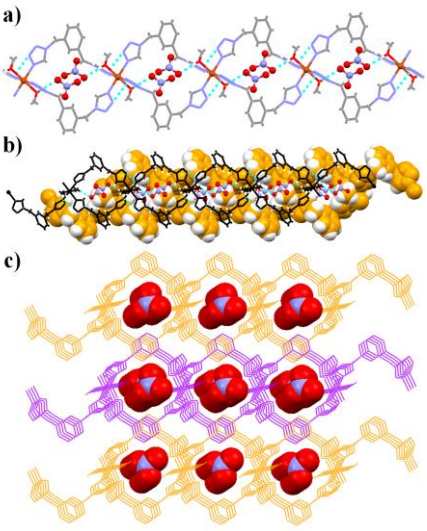

Figure 8: Crystal structure illustration of **4**; a) the looped chain CP in **4**; the hydrogen bonding interaction involving the nitrate anion and metal bound MeOH also displayed; b) offset packing of the looped chains supported by various hydrogen bonding and other weak interactions; c) occlusion of nitrate anion within the cavities of the lopped chain CP.

As a part of our ongoing research on the synthesis of novel MOFs, we are fascinated in studying the supramolecular structural diversities in MOFs and their affecting forces (*e.g.* H-bonding, anions, ligating topology, *etc.*) as well as functional properties (*e.g.* spin crossover (SCO) behaviour, sorption properties, *etc.*[33]). Recently we have reported a remarkable three dimensional chains of nanoballs derived from $Cu(BF_4)_2$ and 2-(4*H*-1,2,4-triazol-4-yl)acetic acid. The crystal structure analysis revealed that the self-assembly of the C_3-symmetric, μ^3-O bridged triangular tricopper SBU is the main driving force for the formation of nanoballs with a void size of ~1 nm and total solvent accessible volume of 4477.5 $Å^3$, which accounts for 48% of the cell volume.[33a] We have also reported a novel chiral helicate, derived from a triazole-carboxylate ligand and $CdCl_2$.[33b]

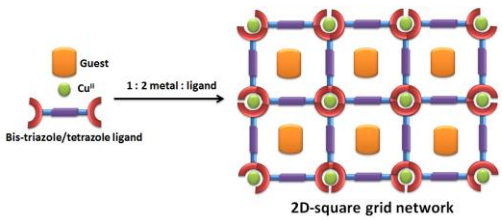

Scheme 6: Schematic representation of the template effect of the guest molecule on the resultant supramolecular architecture of the CP

Encouraged by these results and with the aim to obtain new porous MAFs, herein we present the possibility of various dimensionality of CPs (1D, 2D and 3D) for multi-functional property such as molecular magnetism and gas storage/separation, by reacting with bis-triazole/tetrazole ligands with Cu^{II} metal ions in various stoichiometric ratios. The counter anion and ligands may act as "template", which eventually drive the formation of the resultant supramolecular architecture of the MOFs. This might be crucial for the creation of new supramolecular host aggregates for the incoming guest molecules and moreover, the template effect of the guest molecule on the resultant MOF structure (Scheme 6) is well known.[34] Thus we reacted two bis-triazole/ tetrazole ligands with Cu^{II} salts ($Cu(NO_3)_2$ and $Cu(ClO_4)_2$) separately in 1 : 1, 1 : 2 and 1 : 3, metal : ligand stoichiometric ratio.

Reaction of bis-tetrazole and bis-triazole ligands with $Cu(NO_3)_2$ and $Cu(ClO_4)_2$, respectively, lead to 1D looped chain coordination polymer $\{[Cu(\mathbf{L9})_2(MeOH)_2]\cdot(NO_3)_2\}_\infty$ (**4**) and 2D-square grid coordination polymer $\{[Cu(\mathbf{L10})_2(H_2O)_2]\cdot(\mathbf{L10})(ClO_4)_2\}_\infty$(**5**). The IR spectra of **L9** and **L10** contain characteristic bands at 3116 and 3124 cm^{-1}, corresponding to CH fragments of the tetrazole and triazole groups, respectively. IR spectra of **4** and **5** each contain a broad band for the water and methanol molecules centered at 3390–3400 cm^{-1}. A band for the tetrazole and triazole CH groups was found at 3122 and 3112 cm^{-1} in the spectra of **4** and **5**, respectively. Reaction of **L9** with $Cu(NO_3)_2$ in methanol lead to 1D looped chain coordination polymer namely $\{[Cu(\mathbf{L9})_2(MeOH)_2]\bullet(NO_3)_2\}_\infty$(**4**). IR spectra of **L9** contains characteristic band at 3116 cm^{-1}, corresponding to the tetrazole C–H group and in **4**, 3160 cm^{-1} and 1382 cm^{-1} corresponds to tetrazole C–H and nitrate counter anions, respectively in **5**. SXRD analysis of **4** revealed that it belongs to the triclinic *P*ī space group. The asymmetric unit was comprised of a Cu^{II}, one molecule of ligand **L9** and methanol – both are coordinated to the Cu^{II} metal center. Cu^{II} displays a slightly distorted octahedral pyramidal geometry [∠N–Cu–N = 88.89(7)–91.11(7) º, ∠N–Cu–O = 85.79(6)–94.21(6)º]; the equatorial positions of the metal center are coordinated by the tetrazole N atoms and the apical positions are occupied by methanol molecule. The extended coordination of the bis-tetrazole ligand (**L9**) lead to the formation of 1D looped chain coordination polymer (Fig. 8a). The polymeric chains recognize the counter anion via O-H···O hydrogen bonding involving the metal bound methanol molecule and the counter anion nitrate [O···O = 2.696(5)Å; ∠O–H···O = 172.52°]. Such chains are packed on top of each other in a slightly off-set fashion sustained by various intermolecular interactions (Fig. 8b). It is revealed from the overall packing of the looped chains along the crystallographic axis "a" that the template effect of the nitrate anion is one of the crucial factors for the formation of such chains in **4** (Fig.8c).

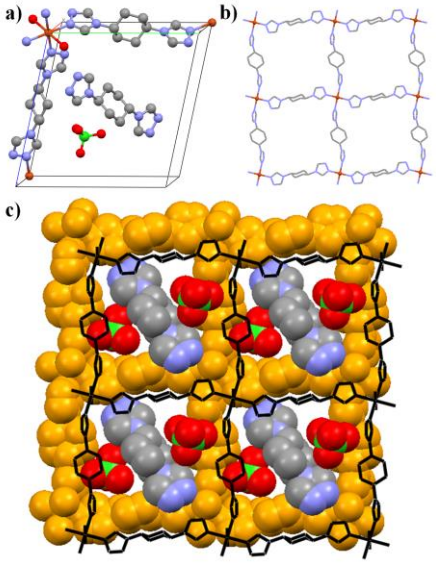

Figure 9: Crystal structure illustration of **5**; a) asymmetric unit of **2**; b) the square grid architecture in **5**; c) stacking modes of the square grids [adjacent grids are shown with orange (space-fill) and black (wireframe)]; occlusion of perchlorate anions and ligand molecules within the channels sustained by hydrogen bonding are also displayed.

Compound **5** crystallizes in the centrosymmetric space group *P*ī. The asymmetric unit (Fig. 9a) contains one perchlorate anion, one ligand molecule (**L10**) centered on the (½, ½, ½) site and one Cu^{II} ion situated at the crystallographic cell origin and bonded to two ligands moieties and a water molecule. Each entity is generated in its entirety by the corresponding centers of the inversion. The unit cell content is $Cu(C_{10}H_{14}N_6)_2(H_2O)_2.2(ClO_4).C_{10}H_{14}N_6$. Thus, each Cu^{II} ion which is linked to four ligands and two water molecules is surrounded by four N and two O atoms. Such a coordination environment of the

Cu^{II} adopts the shape of a regular octahedron which is defined by only two Cu-N distinct bond lengths (Cu–N4 = 2.014(2) Å and Cu–N1 = 2.035(2) Å), one Cu–O bond length (Cu–O1 = 2.431(3) Å) and the corresponding angles (N4–Cu–N1 = 89.42(9)°, N4–Cu–O1 = 85.20(10)° and N1–Cu–O1 = 91.53(11)°).The Cu^{II} atoms are bridged by the ligands creating a polymeric structure in a two dimensional network (Fig. 9b). The boughs formed by the ligands which link the copper atoms within a same layer are parallel to the [110] or to the [101] directions so as the 2D sheets are parallel to the (-111) crystallographic plane (Fig. 9c). As a result, the shortest Cu–Cu distances do not bring into play copper atoms from a same layer: the interlayer Cu–Cu shortest distances correspond to the *a* (6.5086(4) Å), *b* (12.4962(8)Å) and *c* (12.9374(8)Å) cell parameters and the intralayer Cu–Cu shortest distances corresponds to the diagonal of the (*ab*) and (*ac*) planes (13.838(1)Å and 13.978(1)Å, respectively). The average planes of the triazole entities from the same bough are all parallel for symmetrical reasons while the angle between the average plane of each triazole entity that belongs to a bough parallel to [101] and the average plane of a triazole entity that belongs to a bough parallel to [110] is 167.4(1)°. The sheets are stacked along the "*a*" direction and are deduced from each other by a simple period translation, which results in the formation of real channels (Fig. 9c). The shape of the section of such tubes is almost a square with a surface of around 195 $Å^2$. These tubes can also be seen as infinite chains of cavities delimited by the ligands boughs, the volume of the cavities being, for symmetrical reasons, equal to the volume of the crystallographic cell (1022 $Å^3$). Each of these cavities is filled with one ligand molecule and two perchlorate anions (Fig. 9c). The layers are linked to the guest molecules by H-bonding between the water molecules and the nitrogen atoms of the ligand [O1···N8 = 2.857(1) Å, H1A···N8 = 2.035(1)Å, O1–H1···N8 = 168(1)°] and between the ligands and the perchlorate anions [C2···O3 = 3.401(5)Å, H2···O3 = 2.527(5)Å, C2–H2···O3 = 157(1)°]. The perchlorate anions are also involved in H-bonding with the ligand molecules with the same cavity [C11–O5 = 3.372(5)Å, C11–H11···O5 = 169(1)°]. No relatively short distances are created between neighboring cavity contents.

CO_2 sorption studies: Inspired by the 2D square grid structure with occluded guest ligand in **5**, we thought that if we start synthesis with 1:2 metal:ligand ratio, we may end up with an identical structure without guest ligand. Such kind of grid structure could be nice candidate for CO_2 sorption. Indeed, we could synthesized such porous CP (**6**), for which a model structure is shown on Fig. 10a. The CO_2 sorption isotherms of the complex were measured at 303 K up to 24.79 bar. The CO_2 adsorption–desorption isotherm (Fig.10b) exhibits Type-I sorption behavior according to Brauner classification, typical for adsorption in microporous materials. This type of isotherm shows an initial steep increase, corresponding to progressive filling of the micropores, and then a plateau is reached at higher pressures, corresponding to monolayer coverage. Indeed, for microporous materials the small pore dimensions of the adsorbent limit the adsorption only to one or a few molecular layers. The Langmuir model describes Type-I isotherms with a kinetic approach and assuming that the adsorption enthalpy is independent from the coverage. The CO_2 adsorption isotherm was reversible with pressure which means that the adsorbed hydrogen can be easily desorbed by reducing the pressure. Also the shape of isotherm shows that CO_2 sorption capacity was not saturated at 1,20 bar pressure; higher CO_2 sorption capacities can be obtained by increasing the hydrogen adsorption pressure.

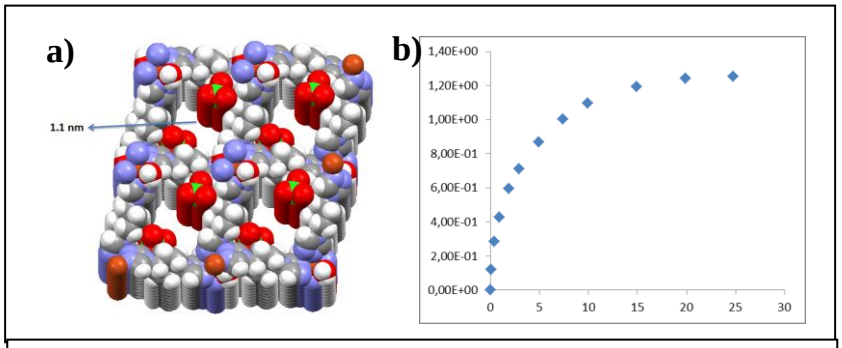

Figure 10: a) Propose model structure of **6**; b) CO_2 adsorption–desorption isotherm of **6**

Conclusion: In summary, a crystal engineering based design strategy for the design of new Cu^{II} metal azole frameworks, where the templating effect of anion or ligand on the resultant structure of coordination polymer has been demonstrated by discovering a two CPs **4** and **5**. While in CP **4**, NO_3^- anion acts as a template (NO_3^- anion got entrapped within the cavity of the looped chain CP in **4**), in CP **5** both anion (ClO_4^-) and ligand templated the formation of the square grid architecture (both ClO_4^- anion and the ligand **L10**, got entrapped within the channels of the square grid CP in **5**). More interestingly **6** (the guest excluded isomorphous of **5**) exhibit type-I CO_2 sorption, according to Brauner classification, typical for adsorption in microporous materials.

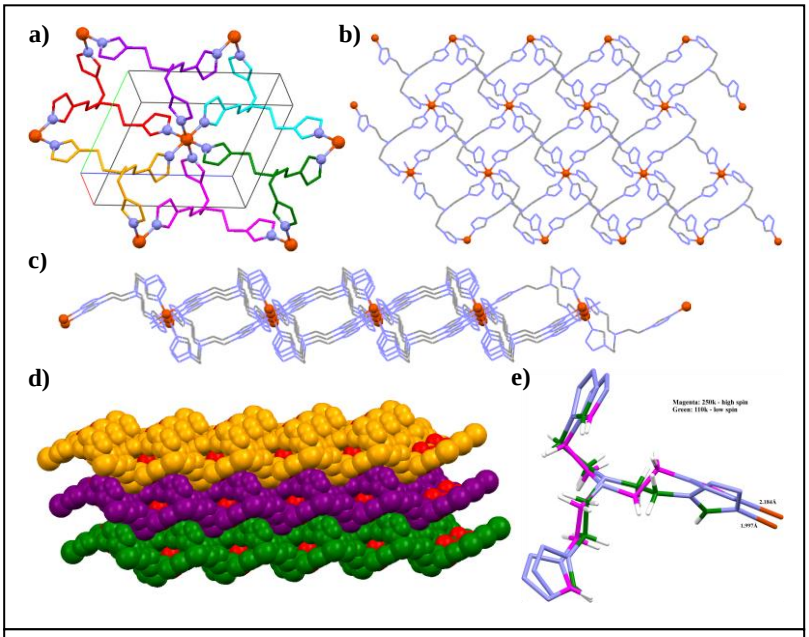

Figure 11: Crystal structure illustration of **7**; a) FeN_6 chromophore in **7**; b) 2D-corrugated sheet like MOF in **7**; c) stacking modes of the 2D-corrugated sheet; d) occlusion of perchlorate anions (red) within the interstitial space of 7; adjacent sheets are shown with orange, purple and green; e) Overlay of **L11** conformations as observed in various temperatures (magenta - 250K HS; green – 110K LS)

2.2.4 A crystal engineering rationale in designing a Fe^{II} spin-crossover MOFs derived from a tris-tetrazole ligand*

(*this work has been completed during project extension period: 18th April-18th July)

Spin-crossover (SCO) molecular switches derived from MOFs have emerged as remarkable switchable materials. Developing new strategies that allow the tailoring of such functional materials with predictable architecture and properties is an important objective and current interest of materials science. However, detailed knowledge on the structure-property correlation is still scanty due to the few number of crystal structures of such compounds so far reported. Therefore we propose a crystal engineering based design strategy to synthesize novel SCO Fe^{II} MOFs.[32] In this attempt, our goal is to develop novel Fe^{II} MOFs derived from triazole/tetrazole ligands capable for SCO property and determine factors affecting their resultant magnetic property. Our design strategy is based on synthesize new 1,2,4-triazole/tetrazole ligands capable for nourishing both rigidity between spin centers of FeN_6 chromophore with an appropriate ligand field, and a dense supramolecular two dimensional network in their crystal lattice to facilitate SCO cooperativity which are very important factors to obtain wide bistability domains suitable for potential applications in display and data recording devices. For this purpose, we reacted the tren based tetrazole ligand namely tris[2-(1H-tetrazol-1-yl)-ethyl]amine (**L11**) separately with $Fe(ClO_4)_2$ and $Fe(BF_4)_2$ in 1:2 metal:ligand ratio and the isolated crystalline products were subjected to single crystal X-ray diffraction. The single crystal structures of two Fe^{II}-MOFs of **L11**

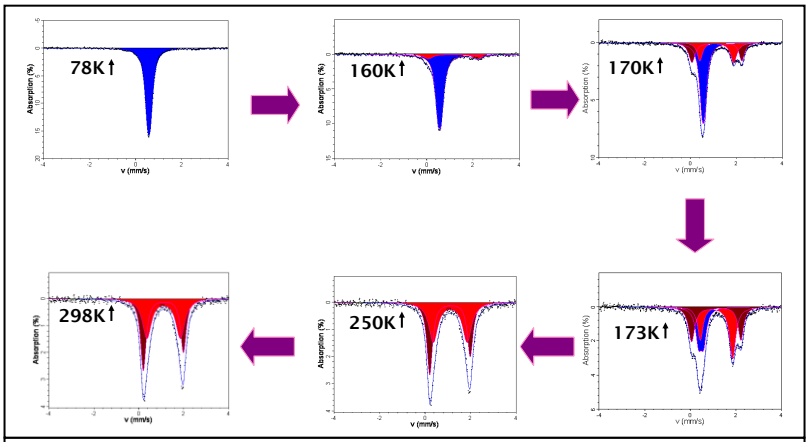

Figure 12: Mössbauer spectra of **7** at various temperatures (LS-blue; HS1 – purple; HS2 – red)

thus obtained have been discussed in this article in the context of structure-property correlation with SCO phenomena. The trials for crystallization of Fe^{II}-MOFs of **L11** from MeOH and EtOH failed as it resulted in the crystallization of the ligand **L11** in almost all the cases. Aqueous acetonitrile solvent systems and 1:2 metal:ligand ratio finally resulted in the formation of two Fe^{II}-MOFs as colorless crystals, namely {[Fe(**L11**)$_2$](ClO$_4$)$_2$} (**7**) and {[Fe(**L11**)$_2$](BF$_4$)$_2$} (**8**). The formulation of **7** and 8 was confirmed by elemental analysis and single crystal structure. Both **7** and **8** were considerably more stable, and in a nitrogen atmosphere, the first symptoms of decomposition (crystals becoming cloudy) arise after a few weeks. The Fe^{II} MOFs **7** and **8** exhibit thermochromism; on cooling, with pronounced color change from white to purple indicating the occurrence of the HS→LS transition. The FT-IR spectra of **7** and **8** contain characteristic bands at 3116 and 3114 cm^{-1}, corresponding to CH fragments of the tetrazole group, respectively. Single crystal X-ray diffraction measurements of **7** and **8** were performed at 250 and 110 K (heating mode). Both compounds are isomorphous and belong to the triclinic *P*ī space group. The asymmetric unit was comprised of a Fe^{II}, one molecule of ligand **L11** –coordinated to the Fe^{II} metal center. At 250 K the Fe–N bond lengths are in the range of 2.175(5)–2.204(5) in **7**, characteristic for the high-spin form of Fe^{II} ions. The metal center Fe^{II} displayed a slightly distorted octahedral pyramidal geometry [∠N–Fe–N = 88.87(19)–90.53(19)º]; both the equatorial and axial positions of the metal center are coordinated by the tetrazole N atoms lead to the formation of FeN_6 chromophore in which one **L11** molecule bridges three Fe^{II} ions and, simultaneously, the six **L11** molecules are coordinated to the one central atom (Fig. 11a). The extended coordination of such FeN_6 chromophore, lead to the formation of 2D-corrugated sheet like MOF (Fig. 11b and 11c). Such corrugated sheets are packed on top of each other in an offset fashion mediated by various supramolecular interactions (π…π stacking) involving the tetrazole rings. The counter-anion perchlorate or tetrafluoroborate were present within the interstitial space between two corrugated sheets and are involved in hydrogen bonding and other weak interactions with the tetrazole rings and perchlorate anion (Fig. 11d). In **7** and **8** the topology of the network originates from the coordination geometry of the iron(II) ions, and also here an orientation of the Fe-N bonds is incompatible with the directions of the network propagation. The unit cell contains no voids accessible for the solvent molecules. Unexpectedly, at 110 K significant differences in the Fe-N bond length was observed in both compounds; Fe-N distance short up to the range of 1.992(2)-1.998(2), a characteristic range for LS compounds. The temperature-dependent magnetic susceptibility measurements for **7** were performed over the 78-298 K range using Mössbauer spectrometer. Selected Mössbauer spectra are displayed in Fig. 12. At 78K, the spectrum of **7** consists of only one quadrupole doublet with isomer shift δ = 0.56903(66) mm/s and quadrupole splitting, ΔE_Q = 0.1297(26) mm/s corresponds to the LS state of Fe^{II}. Upon warming to 298 K, the area fraction of the HS doublet slowly increases until it reaches 100%, confirming a thermally induced LS → HS complete conversion; interestingly two different Fe^{II} HS sites were observed with isomer shifts δ = 1.0473(24) and 1.0614(30) mm/s, and quadrupole splitting ΔE_Q = 1.5893(70) and 1.3595(85) mm/s, respectively. Thermodynamic parameters for the SCO event in **7** was evaluated from differential scanning calorimetry (DSC) measurement. An endothermic peak was observed on warming at $T^{\uparrow max}$ = 173 K and an exothermic peak is recorded at $T^{\downarrow max}$ = 154 K, on cooling (Fig. 13). δ and ΔE_Q of both LS and HS species are typical of an $Fe^{II}N_6$ coordination polymer in which iron centers are bonded by triple *N*1,*N*2-triazole bridges.

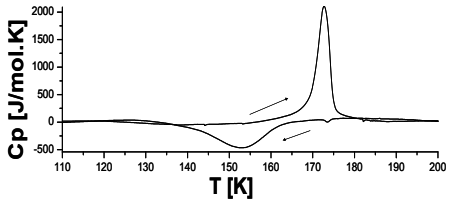

Figure 13: Heat capacity profiles for **7** derived from DSC at 10 K/min. The arrows indicate the cooling (←) and warming (→) modes, respectively.

2.2.5 Fe^{II} SCO CP derived from m-xylylene-bis(1,2,4-triazole) ligand (*this work has been done during project extension period: 18th April-18th July)

SCO CPs are among the most fascinating materials in the field of molecular magnetism because they may show hysteresis at room temperature conferring a memory effect to the material. The switching between the HS and LS states may be triggered by different external stimuli such as light, temperature, pressure, magnetic field, etc. On cooling, these CPs usually exhibit thermally induced gradual spin conversions. In certain cases, abrupt spin transitions with hysteresis effects, whose width strongly depends on the nature of the molecular bridge between Fe^{II} sites as well as on crystal packing, are observed. The Fe^{II} SCO phenomenon involves an entropy driven intra-ionic electron transfer from a diamagnetic low-spin (LS) state to a paramagnetic high-spin (HS) state which is reversibly induced by external stimuli like temperature, pressure and light irradiation *etc*. Derivatives of 4-substituted-1,2,4-triazole have long been an attractive scaffold in the design of such SCO compounds due to their diverse binding modes and bridging properties resulting in topologies varying from mononuclear complexes to high dimensional coordination polymers. In this section we present a novel Fe^{II} SCO CP derived from a bis-triazole ligand namely, m-xylylene-bis(1,2,4-triazole). The reaction of $Fe(ClO_4)_2$ with m-xylylene-bis(1,2,4-triazole) in 1:3 metal : ligand ratio in water resulted in the precipitation of CP namely $\{[Fe(\mathbf{L12})_3].(ClO_4)_2.(H_2O)_2\}$ (**9**) (Scheme 7); the formulation is based on elemental analysis. SEM image on bulk sample of **9** shows highly aggregated amorphous granules that is confirmed by a poor XRPD pattern. Inclusion of non-coordinated perchlorate anion is confirmed by the strong characteristic band around 1,095 cm^{-1}. **9** exhibits a reversible thermochromism to dark pink upon cooling to $N_2(l)$ giving a good indication to the presence of SCO. Selected Mössbauer spectra are displayed in Fig. 14. At 78K, the spectrum of **9** consists of two quadrupole doublets of different resonance area fractions. The major quadrupole doublet (78%) with δ = 0.55 mm/s and ΔE_Q = 0.33 mm/s corresponds to the LS state of Fe^{II}. The presence of a LS quadrupole splitting stems from a lattice contribution to the electric field gradient and therefore reveals a distorted character for the LS octahedron as expected for a constraint one within a 1D chain with a rigid linkage. Another doublet, corresponding to HS Fe^{II} ions (22%), with δ = 1.16 mm/s and ΔE_Q = 3.24 mm/s confirms the incomplete nature of the ST at 77 K. Upon warming to 298 K, the area fraction of the HS doublet slowly increases until it reaches 81%, confirming a thermally induced LS → HS conversion. This conversion is incomplete, which is due to the presence of 19% of LS species. Differential scanning calorimetry of **9** does not showed any signal which indicates gradual ST without any hysteresis. The temperature variation of δ^{HS}, of **9**, reveals a slight linear increase on cooling which is attributed to the second order Doppler shift. δ and ΔE_Q of both LS and HS species are typical of an $Fe^{II}N_6$ coordination polymer in which iron centers are bonded by triple *N*1,*N*2-triazole bridges.

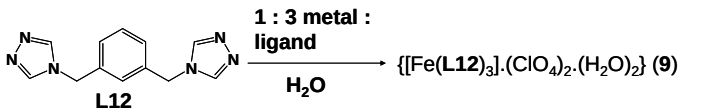

Scheme 7

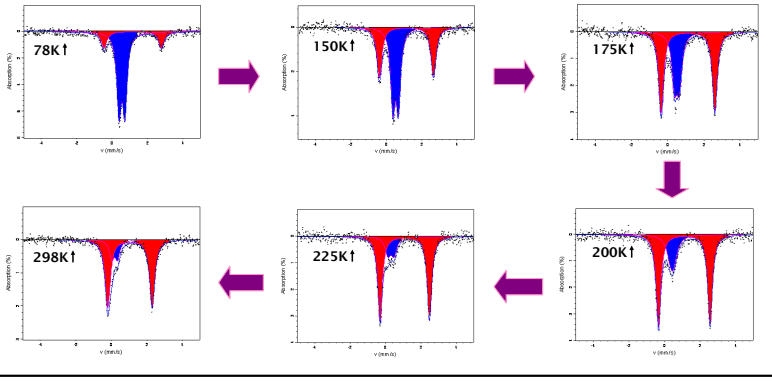

Figure 14: Mössbauer spectra of **9** at various temperatures (LS-blue; HS – red)

3. Conclusion

Thus, we have synthesized a new series of triazole/tetrazole ligands **L1-L12** derived from chiral L-amino acids and achiral compounds. We have explored the multidentate 1,2,4-triazole ligand **L1** to search for a SWMONT by reacting with $CuSiF_6$. Interestingly **L1** formed unprecedented single-walled metal-organic nanotube **1** which is one of the first examples of SWMONT derived from an amino acid backbone. We have also explored the ligand **L2** to synthesize novel Cu^{II} metal-azole grids **2** and **3.** Thus we established, that the nature of the anion in the starting salt (SiF_6^{2-} in **2** and Cl^- in **3**) influences significantly onto the structure of the resulting metal-azole framework. The strong anti-ferromagnetic property of **2** and **3** were also studied. A crystal engineering based design strategy for the design of new Cu^{II} metal azole frameworks, where the templating effect of anion or ligand on the resultant structure of coordination polymer has been demonstrated by discovering a two CPs **4** and **5**. While in CP **4**, NO_3^- anion acts as a template (NO_3^- anion got entrapped within the cavity of the looped chain CP in **4**), in CP **5** both anion (ClO_4^-) and ligand templated the formation of the square grid architecture (both ClO_4^- anion and the ligand **L10**, got entrapped within the channels of the square grid CP in **5**). More interestingly **6** (the guest excluded isomorphous of **5**) exhibit type-I CO_2 sorption, according to Brauner classification, typical for adsorption in microporous materials. We have also designed and synthesized a series of Fe^{II} spin crossover coordination polymer **7-9** derived from a tripodal-tetrazole ligand (**L11**) and bis-triazole ligands; and characterized by various techniques including Mössbauer spectroscopy. **7** and **8** showed thermal induced SCO in a hysterics fashion; while **9** exhibit incomplete ST.

4. Acknowledgment

We thank Belgium Science Policy (BELSPO) for financial support and for a Marie Curie IAP postdoctoral research fellowship for N.N.A.

5. References

1 (a) H. Deng, S. Grunder, K. E. Cordova, C. Valente, H. Furukawa, M. Hmadeh, F. Gándara, A. C. Whalley, Z. Liu, S. Asahina, H. Kazumori, M. O'Keeffe, O. Terasaki, J. F. Stoddart, O. M. Yaghi, *Science*, **2012**, *336*, 1018; (b) Kitagawa, S. Kitaura, R., Noro, S. *Angew. Chem. Int. Ed.* **2004**, *43*, 2334-2375.

2 A. D. Naik, J. Marchand-Brynaert, Y. Garcia, *Synthesis*, **2008**, *1*, 149.

3 (a) H. Tezer, M. Erkocoglu, A. Kara, B. Bayakci, A. Düzova, O. Teksam, S. Aysun, *Eur. J. Pediatr*. **2011**, *170*, 397. (b) Mercury Update: Impact of Fish Advisories, EPA Fact Sheet. EPA-823-F-01-011, EPA, Office of Water, Washington, DC, **2001**.

4 (a) S. Chiarle, M. Ratto, M. Rovatti, *Water Res*. **2000**, *34*, 2971–2978; (b) R. S. Vieira, M. M. Beppu, *Water Res*. **2006**, *40*, 1726–1734; (c) M. Velicu, H. Fu, R. P. S. Suri, K. Woods, *J. Hazard. Mater*. **2007**, *148*, 599–605; (d) X. Ying, Z. Fang, *J. Hazard. Mater. B* **2006**, *137*, 1636–1642; (e) C. Miranda, J. Yáñez, D. Contreras, R. Garcia, W.F. Jardim, H. D. Mansilla, *Appl. Catal. B: Environ*. **2009**, *90*, 115–119.

5 (a) I. Beurroies, M. Boulhout, P. L. Llewellyn, B. Kuchta, G. Férey, C. Serre, R. Denoyel, *Angew. Chem. Int. Ed*. **2010**, 49, 7526 –7529; (b) A. V. Neimark, F-X. Coudert, C. Triguero, A. Boutin, A. H. Fuchs, I. Beurroies, R. Denoyel, *Langmuir*, **2011**, *27*, 4734–4741.

6 (a) N. N. Adarsh, M. M. Dîrtu, A. D. Naik, A. Léonard, B. Tinant, B. –L. Su, Y. Garcia, *Sequestering inorganic mercury within an unprecedented single-walled metal organic nanotube*, Poster presented in 7th Belgium Crystallographic Symposium – BCS 7 on 10th October **2012** at the Academy House - Hertogsstraat 1 - 1000 Brussels. (b) A. P. Railliet, N. N. Adarsh, A. D. Naik, K. Robeyns, R. Clérac, Y. Garcia, *Cu^{II} Metal-Azole Frameworks derived from a simple triazole-carboxylic acid ligand*, A poster presented at Société Royale de Chimie meeting on 11th October **2012** at Université Catholique de Louvain, Belgium. (c) A. D. Naik, M. M. Dîrtu, A. Leonard, B. Tinant, J. Marchand-Brynaert, B-L. Su, Y. Garcia, *Cryst. Growth Des*., **2010**, 10, 1798–1807.

7 N. N. Adarsh, P. Dastidar, *Chem. Soc. Rev*. **2012**, *41*, 3039-3060.

8 P. Thanasekaran, T-T. Luo, C-H. Lee, K-L. Lu, *J. Mater. Chem*. **2011**, *21*, 13140-13149.

9 (a) M. O'Keeffe, O. M. Yaghi, *Chem. Rev*. **2012**, *112*, 675–702; (b) T. Uemura, N. Yanai, S. Kitagawa, *Chem. Soc. Rev*. **2009**, *38*, 1228-1236; (c) C. Janiak, J. K. Vieth, *New J. Chem*. **2010**, *34*, 2366–2388; (d) A. C. McKinlay, R. E. Morris, P. Horcajada, G. Férey, R. Gref, P. Couvreur, C. Serre, *Angew. Chem*. **2010**, *122*, 6400 – 6406.

10 (a) M. Eddaoudi, D. B. Moler, H. Li, B. Chen, T. M. Reineke, *Acc. Chem. Res*. **2001**, *34*, 319-330; (b) D. J. Tranchemontagne, J. L. Mendoza-Cortés, M. O'Keeffe, O. M. Yaghi, *Chem. Soc. Rev*. **2009**, *38*, 1257-1283.

11 (a) R. Ameloot, L.S., J. Fransaer, L. Alaerts, B. F. Sels,D. E. De Vos, *Chem. Mater*., **2009**. *21*, 2580-2582; (b) N. Campagnol, T.V.A., T. Boudewijns, J. F M Denayer, K. Binnemans, D. E. De Vos and J. Fransaer, *J. Mat. Chem*., **2013**, 1, 5827–5830; (c) T. R. C. Van Assche, G.D., R. Ameloot, D. E. De Vos, H. Terryn, J. F.M. Denayer, *Micropore. Mesopor. Mat*., **2012**, 158, 209-213.

12 A. L. Spek, *J. Appl. Crystallogr*. **2003**, *36*, 7.

13 V. A. Blatov and D. M. Proserpio, TOPOS 4.0, A Program Package for Multipurpose Crystallochemical Analysis, www.topos.ssu.samara.ru/

14 (a) E. W. Washburn, *Phys. Rev*. **1921**, *17*, 273. (b) Assuming intrusion only occurs at constant values of contact angle and surface tension.

15 Sheldrick, G.M. *Acta Cryst.* **2008**, *A64*, 112-122.

16 A.L.Spek, *Acta Cryst.* **2009**, *D65*, 148-155.

17 J. W. Steed and J. L. Atwood, *Supramolecular Chemistry*, J.Wiley & Sons, Chichester, 2nd edn, 2009ю

18 (*a*) G. R. Desiraju, J. J. Vittal and A. Ramanan, *Crystal Engineering - A Textbook, World Scientific*, 2011; (*b*) G. R. Desiraju, *Angew. Chem., Int. Ed*., **1995**, 34, 2311; (*c*) G. R. Desiraju, *Angew.Chem. Int. Ed.*, **2007**, 46, 8342.

19 (*a*) H. L. Schläfer and G. Gliemann, *Basic Principles of Ligand Field Theory*, Wiley Interscience: New York; 1969; (*b*) S. Kitagawa, R. Kitaura and S.-I. Noro, *Angew. Chem. Int. Ed*., **2004**, 43, 2334.

20 G. R. Desiraju and T. Steiner, *The Weak Hydrogen Bond in Structural Chemistry and Biology*, Oxford University Press, Oxford, UK, 1999.

21 S. Banerjee, N. N. Adarsh and P. Dastidar, *CrystEngComm*, **2009**, *11*, 746.

22 M. Goel and M. Jayakannan, *Chem. Eur. J*. **2012**, *18*, 2867.

23 F. A. A. Paz, J. Klinowski, S. M. F. Vilela, J. P. C. Tomé, J. A. S. Cavaleiro and J. Rocha, *Chem. Soc. Rev*., **2012**, *41*, 1088.

24 T. Fukushima, S. Horike, H. Kobayashi, M. Tsujimoto, S. Isoda, M. L. Foo, Y. Kubota, M. Takata and S. Kitagawa, *J. Am. Chem. Soc*., **2012**, *134*, 13341.

25 J.-P. Zhang, Y-B. Zhang, J-B. Lin and X-M Chen, *Chem. Rev*. **2012**, *112*, 1001.

26 D. Lässig, J. Lincke, J. Moellmer, C. Reichenbach, A. Moeller, R. Gläser, G. Kalies, K. A. Cychosz, M. Thommes, R. Staudt and H. Krautscheid, *Angew. Chem. Int. Ed*. **2011**, 50, 10344.

27 J. F. Eubank, L. Wojtas, M. R. Hight, T. Bousquet, V. Ch. Kravtsov and M. Eddaoudi, *J. Am. Chem. Soc*. **2011**, *133*, 17532.

28 J. F. Eubank, F. Nouar, R. Luebke, A. J. Cairns, L. Wojtas, M. Alkordi, T. Bousquet, M. R. Hight, J. Eckert, J. P. Embs, P. A. Georgiev and M. Eddaoudi, *Angew. Chem. Int. Ed*. **2012**, 51, 10099.

29 J. Möllmer, M. Lange, A. Möller, C. Patzschke, K. Stein, D. Lässig, J. Lincke, R. Gläser, H. Krautscheid and R. Staudt, *J. Mater. Chem*., **2012**, 22, 10274.

30 (*a*) A. D. Naik, M. M. Dîrtu, A. Léonard, B. Tinant, J. Marchand-Brynaert, B.-L. Su and Y. Garcia, *Cryst. Growth Des*., **2010**, *10*, 1798; (*b*) M. M. Dîrtu, C. Neuhausen, A. D. Naik, A. Léonard, F. Robert, J. Marchand-Brynaert, B.-L. Su and Y. Garcia, *Cryst. Growth Des*., **2011**, 11, 1375; (*c*) A. D. Naik, B. Tinant, A. Léonard, J. Marchand-Brynaert, B.-L. Su and Y. Garcia, *Cryst. Growth Des*., **2011**, *11*, 4034; (*e*) A. D. Naik, J. Beck, M. M. Dîrtu, C. Bebrone, B. Tinant, K. Robeyns, J. Marchand-Brynaert and Y. Garcia, *Inorg. Chim. Acta*, **2011**, *368*, 21; (*f*) Y. Garcia, F. Robert, A. D. Naik, G. Zhou, B. Tinant, K. Robeyns, S. Michotte and L. Piraux, *J. Am. Chem. Soc*., **2011**, *133*, 15850.

31 F. A. A. Paz, J. Klinowski, S. M. F. Vilela, J. P. C. Tomé, J. A. S. Cavaleiro and J. Rocha, *Chem. Soc. Rev*., **2012**, *41*, 1088

32 Y. Garcia, A. D. Naik, N. N. Adarsh, *Chimia*, **2013**, 67, 411.

33 Tanaka, D.; Kitagawa, S. *Chem. Mater*. **2008**, *20*, 922–931.